Chapter 5

Study of optical, structural, physical, and radiative properties of samarium, and praseodymium-based phosphate glass for building envelope, photonic, and optoelectronic applications

5.1 Introduction

Environmental deterioration and energy scarcity highlight the growing significance of new scientific resources and affordable devices in the modern period. These issues can be resolved by rare earth-doped multicomponent phosphate glass systems, which have the potential to be used in ecologically friendly and energy-efficient technology. These rare earth-energized glass systems have attracted much interest due to their potential and wide range of uses in luminous gadgets. Solid-state lasers, optical filters, cathode ray tubes, fluorescent lamps, plasma displays, field emission displays, white light-emitting diodes, traffic signals, automobile displays, cell phone illumination, night-vision goggles, medical diagnostic devices, optical detectors, and sensors make use of them [29-32]. Developing effective optical devices requires selecting the best network structure for the glass matrix doped with rare earth elements. Phosphate glass is a favored material because of its exceptional mechanical, chemical, and thermal stability. Because of their excellent optical properties, which are necessary for various optical applications, rare earth phosphates are especially useful. The main structural components of pure phosphate glasses are PO_4 tetrahedral groups joined by covalent bridging oxygens in the glassy system. Phosphate and fluoride groups have lower phonon energies (1084 cm^{-1} and 580 cm^{-1}, respectively) than traditional silicate (1100 cm^{-1}) and borate (1387 cm^{-1}) groups. Fluorophosphate groups are better suited as rare earth species' host materials for photoluminescence purposes because of their reduced phonon energy. Longer excited state durations and increased quantum efficiency of photoluminescence are facilitated by glasses with lower phonon energy. Phosphate glasses have disadvantages despite

their benefits, such as being vulnerable to hydroxyl (OH) group breakdown. Doping the glass matrix with other elements, such as zinc and fluorine, can lessen these difficulties. In optical applications, these dopants aid in enhancing the stability and functionality of phosphate glasses [33]. When transition metal ions, such as ZnO, are added to glass frameworks, several dopant sites are introduced, improving the glass's optical and spectral characteristics. By acting as a network modifier, ZnO increases the glass matrix's chemical resilience. This alteration improves the glass's general stability in addition to its optical qualities, which makes it more appropriate for a range of uses where improved optical performance and longevity are essential [34]. Glasses can be further improved by adding amounts of heavy metal oxides, such as BaO, Bi_2O_3, PbO, and others, in addition to doping with transition metals or rare earth ions. These heavy metal oxides give the glasses many advantageous qualities.

- Density and Refractive Index: The total density of glass is raised by the greater atomic weights of heavy metal oxides. Additionally, this raises the glass's refractive index, which qualifies it for use in optical applications.
- Chemical Durability: Over time, heavy metal oxides strengthen the glass matrix's resistance to environmental deterioration and chemical attack.
- Resistance Against Devitrification: By adding heavy metal oxides, glass can increase its resistance to crystallization, or devitrification, at high temperatures, guaranteeing stability during usage and processing.
- Lower Processing Temperature: By lowering the processing temperature needed to make the glass, some heavy metal oxides can save production costs and energy usage.

- Phonon Energies: The glass matrix's phonon energies may change if heavy metal oxides are added. Because they contribute to strong and efficient fluorescence, lower phonon energies are preferred for applications like fiber amplifiers and lasers.

Because of these improvements, heavy metal oxide-doped glasses are extremely adaptable and appropriate for a variety of cutting-edge technological applications in photonics, optics, and other fields [**16**,**132**]. Strong emission lines appear when optically active f-f electronic transitions of lanthanide ions are introduced into different glassy substrates. Because of its prospective uses in optical communication and display technologies, glasses doped with Pr ($[Xe]4f^3 6s^2$) and Sm ($[Xe]4f^6 6s^2$) have attracted a lot of interest among rare earth species. Sm^{3+} ions have high energy levels, significant fluorescence intensity, broad emission cross-sections, and excellent quantum efficiency. Because of these qualities, they are especially well-suited to improving already-existing optical characteristics and facilitating the creation of novel optical functions in glasses [**35**]. Because of their unique emission lines from three different energy states-$^3P_0$, $^1D_2$, and $^1G_4$-research on the luminous characteristics of Pr^{3+} ions in glass matrices has garnered a lot of attention. Pr^{3+}-doped glasses are intriguing candidates for a variety of optical applications because of these transitions' strong and distinct spectrum features [**36**]. Motivated by the previously reviewed literature, the current study focuses on creating new compositions of colored fluorophosphate glasses based on PbO that are doped with rare earth (RE) species like Pr^{3+} and Sm^{3+}. Improving their optical and fluorescent characteristics for a variety of uses is the goal. The study uses Judd-Ofelt (JO) theory and a variety of characterization approaches in addition to looking into the optical characteristics and network structures of the glass. The optical, fluorescence, and physical properties of the RE-doped pigmented fluorophosphate glasses under study are directly understood and improved by these efforts.

5.2 Materials and Methods

A conventional melt annealing process was used to create rare earth (Sm, Pr)-doped fluorophosphate glass series featuring molar compositions of (46-x)P_2O_5-15ZnO-15PbO-15K_2O-9CaF_2-xR_2O_3 (where R=Sm, Pr, and x=0, 0.5, 1 mol%). The composition of the base glass that was chosen was 46P_2O_5-15ZnO-15PbO-15K_2O-9CaF_2. Lead monoxide (PbO) from Aldrich Chemical Co., phosphorus pentoxide (P_2O_5), zinc oxide (ZnO), potassium carbonate (K_2CO_3), calcium fluoride (CaF_2), samarium oxide (Sm_2O_3), and praseodymium oxide (Pr_2O_3) obtained from LOBA CHEMIE PVT. LTD was among the chemicals utilized. Every chemical is extremely pure (99% purity). The substances were completely combined in an agate mortar and pestle after being carefully weighed using electronic microanalytical balance equipment with a precision of ± 0.0001 g. To create a uniform glass mixture, batches of about 30 grams were melted in alumina crucibles at 1300°C for ten hours in an electric furnace. After pouring the molten glass onto a hot alumina plate within an iron mold for casting, it was allowed to cool naturally. To alleviate thermal strains and tensions, the glass samples were then annealed at 450°C, followed by progressively cooling to room temperature inside the furnace. The creation of consistent, stable glass samples appropriate for in-depth characterization and ensuing optical and fluorescence investigations is guaranteed by this painstaking procedure. The schematic diagram in **Fig. 5.1** also illustrates all the specific experimental protocols. **Fig. 5.2** shows images of the polished glass samples used for optical and fluorescence characterization.

5.2.1 *Characterization of Materials*

The glass samples were identified and recorded in **Table 5.1** after careful etching to enable spectroscopic investigations. Using the Archimedes principle and water as the immersing fluid,

the density of the generated glass samples was measured. The results showed an estimated variance of about ± 0.003 g cm^{-3} at room temperature. A Jasco V-770 twin-beam UV-VIS , a spectrophotometer (Japan) was used to record the UV and visible spectra of polished glass samples. It was linked to a PC running UV-Win lab software.Fine powders from specific glass samples were subjected to X-ray diffraction (XRD) analysis at room temperature using a Rigaku Smart Lab (9 kW) powder-type X-ray diffraction machine from Rigaku Corporation (Japan). It was outfitted with a Ni filter tube and a graphite monochromatic copper Kα radiation source (λ = 1.540 Å) and ran at 40 kV and 20 mA.

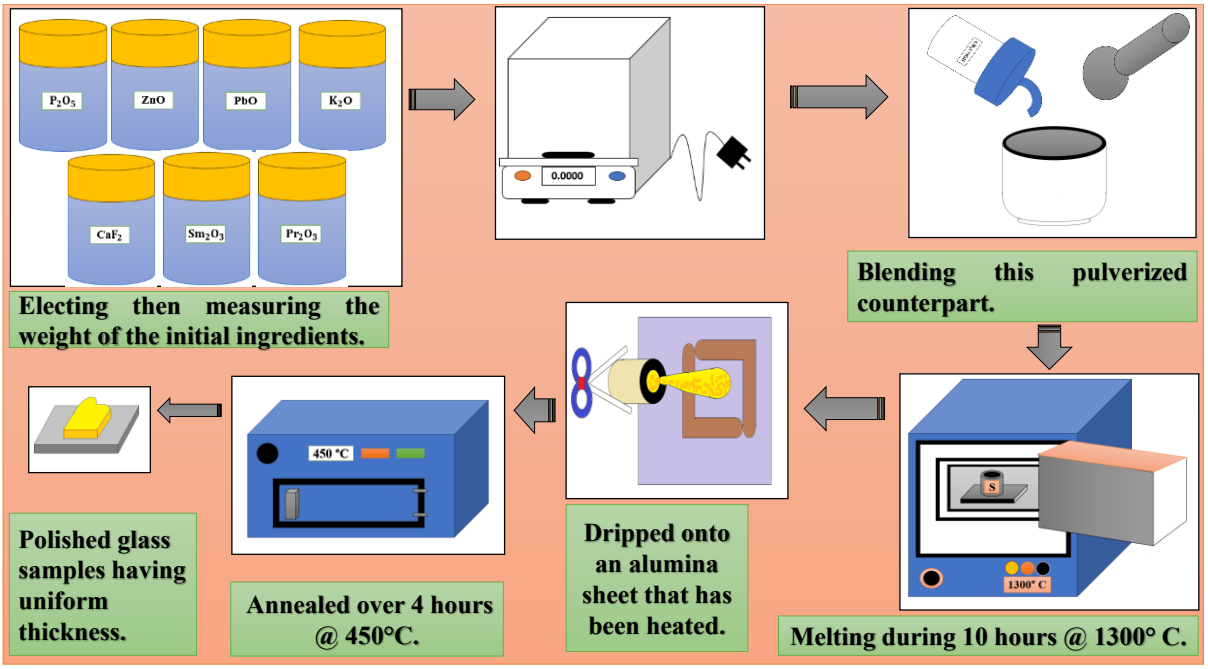

Fig. 5.1. The sample was prepared using the standard melt-quench method outlined in the previous section.

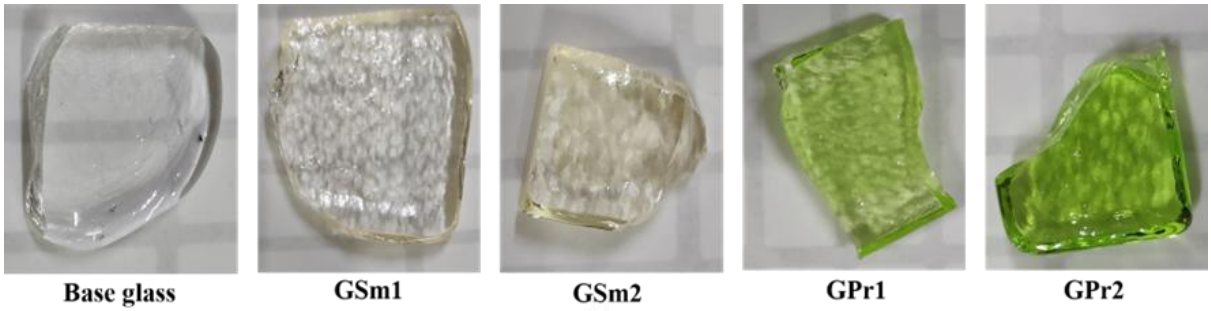

Fig. 5.2. This figure shows photographs of optically polished glass samples prepared for optical and fluorescence analysis, where the base glass has dimensions of 21.42 mm in length, 19.95 mm in breadth, and 6.20 mm in width; GSm1 measures 36.45 mm in length, 27.34 mm in breadth, and 6.00 mm in width; GSm2 has dimensions of 20.79 mm in length, 18.78 mm in breadth, and 7.80 mm in width; GPr1 measures 27.50 mm in length, 16.89 mm in breadth, and 6.40 mm in width; and GPr2 has dimensions of 22.13 mm in length, 19.44 mm in breadth, and 7.70 mm in width.

At a scan rate of 3º min^{-1}, the XRD data were gathered in the 2θ range of 10º to 80º. The acquired patterns were compared with traditional ICDD (International Centre for Diffraction Data) cards for analysis using PANalytical XPert High Score Plus software. Using a Nicolet iS5 FTIR spectrometer from Thermo Electron Scientific Instruments LLC (USA), infrared spectra of the glass samples were obtained in transmittance mode using the KBr disc technique at room temperature, with a resolution of 4 cm^{-1} over the wavenumber range of 4000-450 cm^{-1}. Using a UHTS α-300 confocal-Raman microscope from WITec GmbH (Germany) equipped with a 600 g/mm grating and a 532 nm laser excitation source at 1.5 mW power, the Raman spectra of the base glass and glasses doped with the highest concentrations of samarium and praseodymium were acquired. A WITec α-300 spectrophotometer (Germany) with a 75W xenon lamp source was used to record the fluorescence spectra of the currently chosen glass samples at room temperature. This instrument covered the visible frequency range. The optical, structural, and fluorescent

characteristics of the RE-doped fluorophosphate glasses under study are thoroughly revealed by these detailed spectroscopic analyses.

Table 5.1. The batch compositions (weight percentage) and molar compositions of the glasses that were made.

Glass samples	Molar glass composition	Batch compositions (wt.%)						
		P_2O_5	ZnO	PbO	K_2O	CaF_2	Sm_2O_3	Pr_2O_3
Base glass	$(ZnO)_{15}(PbO)_{15}(K_2O)_{15}(CaF_2)_9(P_2O_5)_{46}$	49.41	9.24	25.34	10.69	5.31	-	-
GSm1	$(ZnO)_{15}(PbO)_{15}(K_2O)_{15}(CaF_2)_9(Sm_2O_3)_{0.5}(P_2O_5)_{45.5}$	48.49	9.16	25.14	10.60	5.27	1.30	-
GSm2	$(ZnO)_{15}(PbO)_{15}(K_2O)_{15}(CaF_2)_9(Sm_2O_3)_1(P_2O_5)_{45}$	47.50	9.10	24.94	10.52	5.23	2.59	-
GPr1	$(ZnO)_{15}(PbO)_{15}(K_2O)_{15}(CaF_2)_9(Pr_2O_3)_{0.5}(P_2O_5)_{45.5}$	47.60	9.10	24.95	10.53	5.24	-	1.23
GPr2	$(ZnO)_{15}(PbO)_{15}(K_2O)_{15}(CaF_2)_9(Pr_2O_3)_1(P_2O_5)_{45}$	46.75	9.03	24.80	10.46	5.20	-	2.44

5.3 Results

All the manufactured glasses with different compositions are found to be transparent. **Fig. 5.1** displays the schematic diagram of the typical melt-quench technique for preparing these glass samples for physical, optical, and photoluminescence assessment. Each glass sample's density (D) was determined using the following formula.

$$D = \frac{W_D \times \rho}{(W_D - W_W)}$$

The results are shown in **Table 5.2**, in which D stands for the glass samples' density, W_D for their dry weight, W_W for their wet weight, and ρ for the density of water-using the following formulas, as cited in Ref. [**133**], the molar volume (V_m), oxygen molar volume (V_O), and oxygen packing density (OPD) of the glass samples under study were calculated and are listed in **Table 5.2**.

$$V_m = \frac{M_{AV}}{D}$$

$$V_O = \frac{V_m}{\sum_i x_i n_i}$$

$$OPD = \frac{(1000 \times k \times D)}{M_{AV}}$$

In this case, k is the number of oxygen atoms per mole in the composition, x_i , and n_i are the molar fraction and number of oxygen atoms of the ith component, respectively, and M_{AV} stands for molar mass. Furthermore, each glass sample's properties, including the concentration of rare earth ions (N), polaron radius (R_p), rare earth ions interionic distance (R_i), and field strength (F), were computed using the following equations, as referenced in [**118**,**133**].

$$N = \frac{X_{RE} \times D \times N_A}{M_{AV}}$$

$$R_p(\dot{A}) = \frac{1}{2}\left(\frac{\pi}{6N}\right)^{1/3}$$

$$R_i(\dot{A}) = \left(\frac{1}{N}\right)^{1/3}$$

$$F = \frac{Z}{R_p^2}$$

The symbols X_{RE} , N_A , and Z stand for the moles (%) of rare earth ions, Avogadro's number, and atomic mass, respectively. **Table 5.2** also provides these parameters. **Fig. 5.3(a)** shows the X-ray diffraction (XRD) spectra of a few chosen glass samples. The amorphous nature of the materials is indicated by the lack of distinct peaks in the 2θ range between 10° and 80°. **Fig. 5.3(b)** displays the Fourier-transform infrared (FTIR) spectra of the basic glass and a few chosen glass samples. There are several vibrational bands visible; most of them are in the fingerprint area. Interestingly, a strong far-IR wideband can be seen at around 1100 cm^{-1}, with medium-sized bands at about 700, 530, and 474 cm^{-1}, as well as a smaller band close to 1632 cm^{-1}. Around 3440 cm^{-1} is the center of a significant intermediate near-infrared band.

Fig. 5.3(c) displays the Raman spectra of the base glass, 1 mol% Sm^{3+}doped glass system (GSm2), and 1 mol% Pr^{3+}doped glass system (GPr2). The Raman band of the base glass is centered at 1042 cm^{-1}. As opposed to the GSm2 glass system, which exhibits bands at 1025 cm^{-1} and 1195 cm^{-1},

the GPr2 glass system exhibits bands at 1025 cm^{-1}, 1207 cm^{-1}, and 1271 cm^{-1}. These thorough spectroscopic analyses show the promise of the RE-doped fluorophosphate glasses under study for a range of technological applications by offering in-depth insights into their physical, optical, and vibrational properties. The weighted mean of experimental data obtained from 360 nm to 830 nm was used to compute the visible and solar optical characteristics of all produced glass samples. Normal incident light was used to perform spectral measurements in the visible and ultraviolet spectrums, including absorption in spectrum mode, transmission in specular transmission mode, and reflection in diffuse reflection mode. In a clean environment, with 20 mm of precipitable H_2O vapor and 3.4 mm of ozone, these measurements were conducted in the average US [37]. The Lambert-Beer equation $\left(I_t = I_0 e^{-\alpha(\omega)t}\right)$ was used to calculate the absorption coefficient α(ω) for each glass sample at different photon energies $\hbar(\omega)$, where t is the sample thickness and I_0 and I_t are the incident and transmitted photon intensities, respectively. **Fig. 5.4(a)** and **Fig. 5.4(b)** show the reflection and transmission spectra in the visible and ultraviolet areas, respectively, of all transparent, cleaned glass samples. The glass samples (GSm1, GSm2, GPr1, GPr2) showed peak transmission intensities around 391 nm, 273 nm, 267 nm, and 395 nm, and peak reflection intensities around 381 nm, 275 nm, 283 nm, and 389 nm, respectively, in the UV range. All glass samples displayed peak reflection and transmission intensities in the visible spectrum at around 860 and 863 nm, respectively.

Table 5.2. Physical properties of the glasses at varying concentrations of samarium and praseodymium oxides.

Physical parameters	Base glass	GSm1	GSm2	GPr1	GPr2
D **(g cm^{-3})**	**3.32**	**3.40**	**3.46**	**3.40**	**3.45**
Thickness(cm)	**0.62**	**0.60**	**0.78**	**0.64**	**0.77**

M_{AV} (g mol^{-1})	13213	13427	13417	13530	13511
V_m (cm^3 mol^{-1})$\times$ 10^{-2}	39.78	39.49	38.77	39.79	39.16
V_O (cm^3 mol^{-1})	14.46	14.46	14.25	14.57	14.39
OPD (g-atm l^{-1})	69.10	69.13	69.55	69.18	69.45
N ($\times$ 10^{20} ions cm^{-3})	0.00	3.05	4.61	3.06	4.61
R_p ($\dot{A}$)	-	5.98	5.21	5.97	5.21
R_i $(\dot{A})$	-	14.85	12.93	14.83	12.94
F ($\times$ 10^{16} cm^{-2})	-	8.56	16.81	8.307	16.06

The following calculations were used to calculate the average weighted values of visible optical properties across the wavelength range of 360 nm to 830 nm.

$$R_{vis} = \frac{\sum_{\lambda=360nm}^{\lambda=830nm} D_\lambda \mu(\lambda) v(\lambda) \Delta\lambda}{\sum_{\lambda=360nm}^{\lambda=830nm} D_\lambda v(\lambda) \Delta\lambda}$$

$$T_{vis} = \frac{\sum_{\lambda=360nm}^{\lambda=830nm} D_\lambda \tau(\lambda) v(\lambda) \Delta\lambda}{\sum_{\lambda=360nm}^{\lambda=830nm} D_\lambda v(\lambda) \Delta\lambda}$$

$$A_{vis} = 100 - R_{vis} - T_{vis}$$

Parameters like wavelength intervals ($\Delta\lambda$), illuminant D65's spectrum distribution (D_λ), spectral luminous efficiency ($v(\lambda)$), spectral reflectance ($\mu(\lambda)$) (%), and spectral transmittance ($\tau(\lambda)$) (%) are all included in these equations.

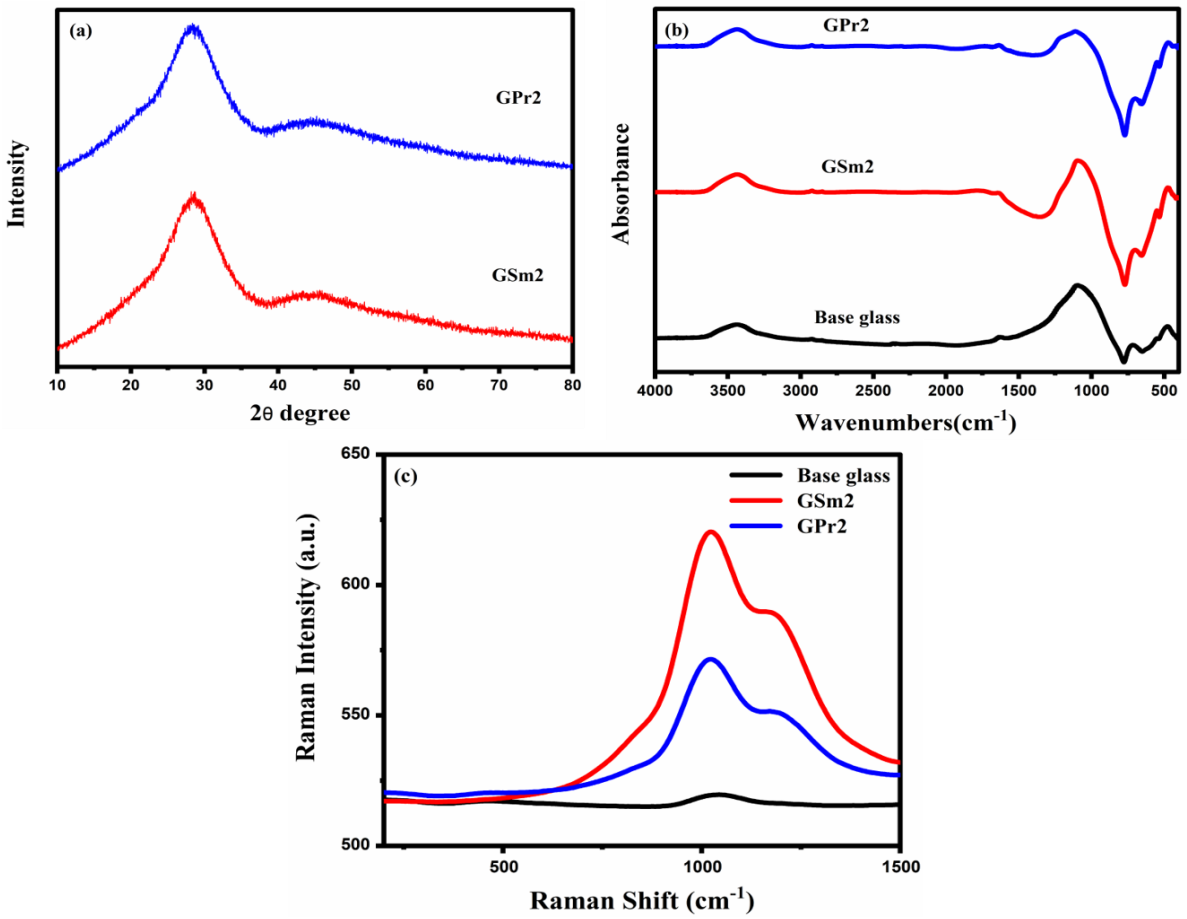

Fig. 5.3. XRD (a), FTIR (b), and Raman (c) spectra of the prepared base glass sample and selected samarium- and praseodymium oxide-doped base glass samples.

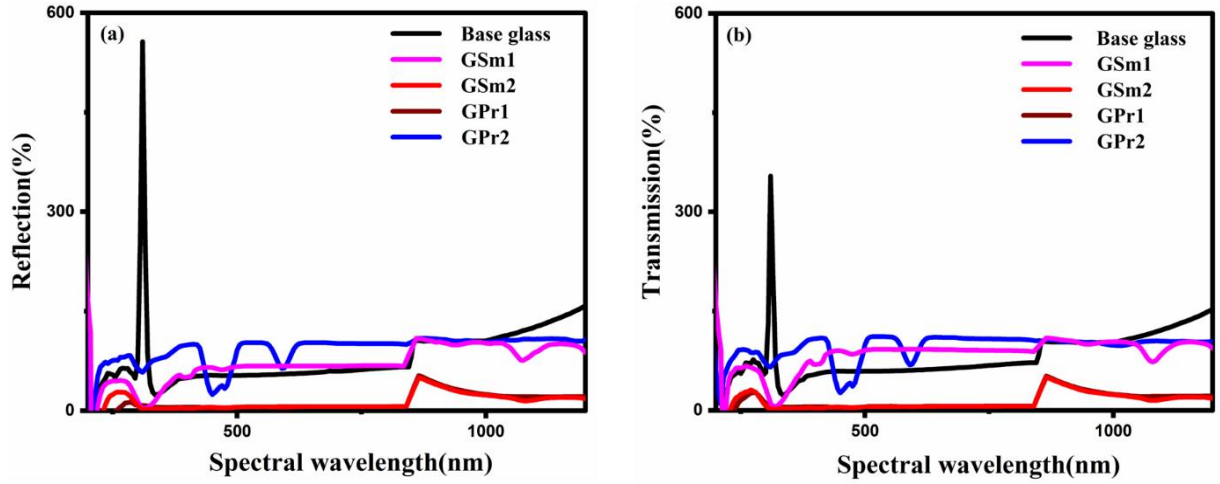

Fig. 5.4. Spectral reflection (a) and transmission (b) curves of lead fluorophosphate glasses doped with Sm^{3+} and Pr^{3+} in the ultraviolet and visible regions.

The following formulas were used to evaluate solar optical characteristics across the entire visible spectrum wavelength range, where S_λ stands for the relative spectral distribution of solar radiation (W/m^2).

$$R_{solar} = \frac{\sum_{\lambda=360nm}^{\lambda=830nm} S_\lambda \mu(\lambda) \Delta\lambda}{\sum_{\lambda=360nm}^{\lambda=830nm} S_\lambda \Delta\lambda}$$

$$T_{solar} = \frac{\sum_{\lambda=360nm}^{\lambda=830nm} S_\lambda \tau(\lambda) \Delta\lambda}{\sum_{\lambda=360nm}^{\lambda=830nm} S_\lambda \Delta\lambda}$$

$$A_{solar} = 100 - R_{solar} - T_{solar}$$

Table 5.3 provides a summary of the calculated visible and solar optical characteristics for each glass sample under study. The following formulas were used to calculate the glass samples' refractive indices (n), taking transmittance (t_s) and absorbance (a) into account.

$$t_s = 10^{-a} \times 100$$

$$n = \frac{1}{t_s} + \sqrt{\frac{1}{(t_s - 1)}}$$

The real $\mathcal{E}_R (\mathcal{E}_R = n^2 + K^2)$ and imaginary $\mathcal{E}_I (\mathcal{E}_I = 2nK)$ components were used to construct the complex dielectric constants, which take into consideration the refractive index (n) and extinction coefficient (K).

The following formulas were used to compute the extinction coefficient (K), which included the absorption coefficient (α).

$$K = \frac{\alpha\lambda}{4\pi}$$

Fig. 5.5 (a), **Fig. 5.5 (b)**, **Fig. 5.5 (c)**, and **Fig. 5.5 (d)** display the dispersion curves for the refractive indices, extinction coefficients, real part of the complex dielectric constant, and imaginary part of the complex dielectric constant for each of the glasses under study, respectively.

The Davis and Mott formula, in which B is a constant, h is Planck's constant, and r is an index number for the electronic transition pathway, was used to calculate the optical energy gap (E_g) of the glass samples.

Table 5.3. Optical properties of fluorophosphate glasses doped with Sm^{3+} and Pr^{3+}.

Optical parameters	Base glass	GSm1	GSm2	GPr1	GPr2
R_{vis}	43.75	42.18	45.93	44.17	47.91
T_{vis}	56.08	57.81	43.84	45.48	51.88
A_{vis}	0.08	0.005	10.17	10.34	0.20
R_{solar}	43.63	42.43	45.86	44.44	48.08
T_{solar}	56.28	57.56	43.76	45.74	51.72
A_{solar}	0.08	0.009	10.37	10.21	0.19
E_{gind} (eV)	3.02	2.90	2.00	2.50	2.45
E_{gd} (eV)	3.65	3.43	2.38	2.62	2.50
E_{urbach} (eV)	0.45	0.27	0.07	0.05	0.16
n_t	2.391	2.424	2.736	2.546	2.563
$R_m \times 10^{-2}$	24.32	24.45	26.5	25.72	25.45
$\alpha_m \times 10^{-2}$	9.650	9.702	10.515	10.206	10.099
R_L	0.168	0.173	0.215	0.19	0.192
T	0.71	0.70	0.64	0.68	0.67
M_c	0.388	0.380	0.316	0.353	0.350
$\Delta\chi^*$	0.811	0.779	0.537	0.672	0.658
$\chi^{(3)} \times 10^{-12}$ (esu)	3.391	3.868	12.095	6.184	6.581
$n_1 \times 10^{-11}$ (esu)	5.34	6.01	16.65	9.15	9.67

$$(\alpha hv) = B\left(hv - E_g\right)^r$$

Tauc's plot, which is shown in **Figs. 5.6(a)** and **5.6(b)** for indirect and direct transitions, respectively, were used to determine the optical band gaps. The optical energy gap results for each glass sample are shown in **Table 5.3**. The following formulas were used to calculate each glass sample's Urbach energy values, shown in **Table 5.3**.

$$\alpha = \alpha_0 \, exp\left(\frac{hv}{E_{\,urbach}}\right)$$

$$ln(\alpha) = ln(\alpha_0) + \left(\frac{hv}{E_{\,urbach}}\right)$$

Fig. 5.6(c) displays the ln(α) vs. hv graphs for each synthesized sample. where E_g is the optical band gap obtained from Tauc's figure.

The following formula was used to get the average refractive index (n_t) of each glass specimen,

$$\left(\frac{n_t^2 - 1}{n_t^2 + 2}\right) = 1 - \sqrt{\frac{E_g}{20}}$$

The Lorentz-Lorenz equation, which is provided below, was used to compute each sample's molar refraction (R_m),

$$R_m = \left(\frac{n_t^2 - 1}{n_t^2 + 2}\right) V_m$$

and the following formula was used to calculate the electronic polarizability (α_m) of the glass sample molecules as a function of molar refraction.

$$\alpha_m = \left(\frac{R_m}{2.52}\right)$$

The following formulas were used to calculate the produced glass samples' optical transmission (T) and reflection loss (R_L) values, respectively.

$$T = \left(\frac{2n_t}{n_t^2 + 1}\right)$$

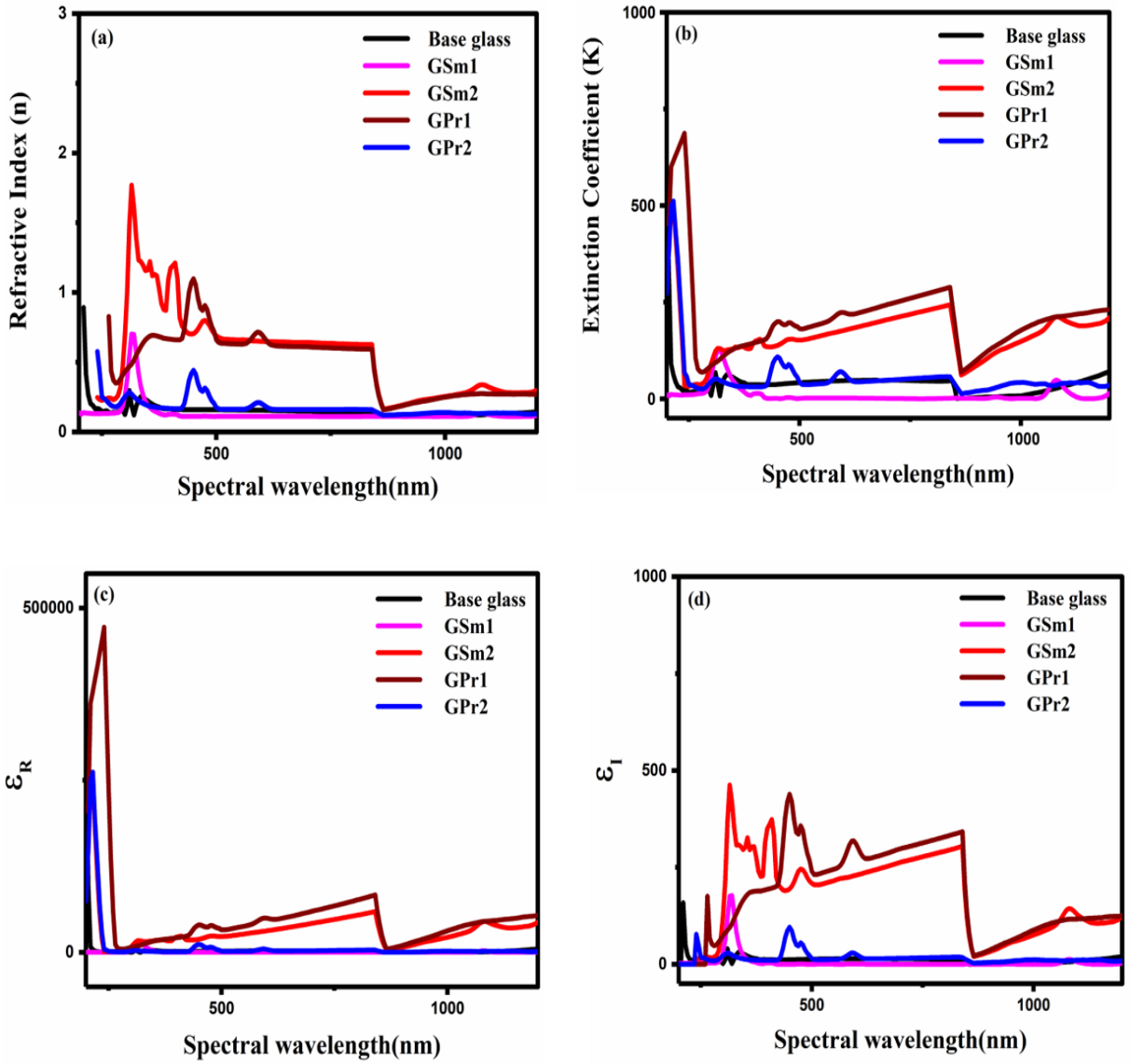

Fig. 5.5. Distribution plots of the refractive index (a), extinction coefficient (b), real part of the complex dielectric constant (c), and imaginary part of the complex dielectric constant (d) as a function of wavelength for all prepared fluorophosphate glass samples doped with Sm^{3+} and Pr^{3+}.

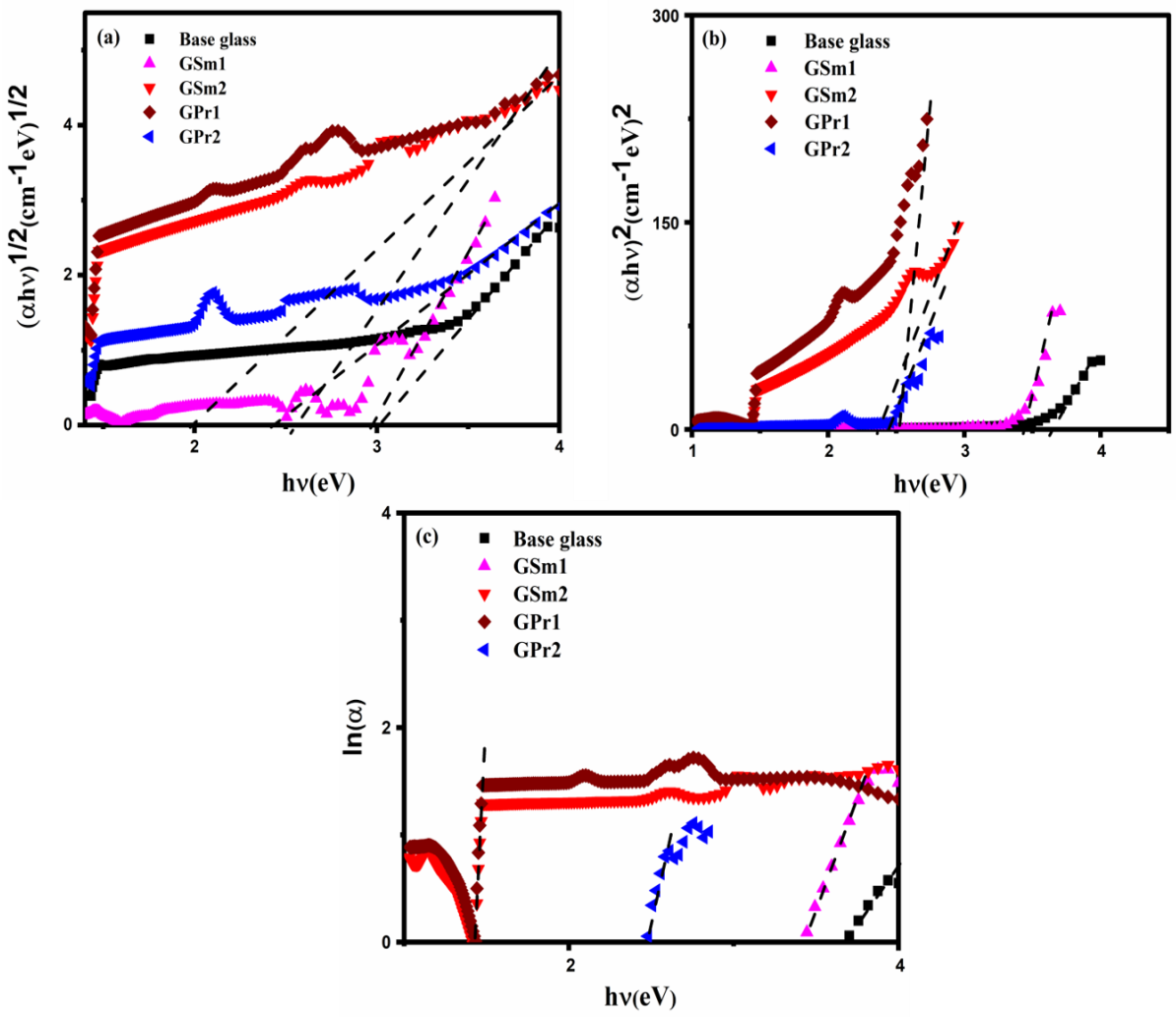

Fig. 5.6. Tauc's plot for selected samples showing indirect transitions (a), direct transitions (b), and the plot of $ln(\alpha)$ versus incident photon energy (hv) for the studied samples (c).

$$R_L = \left(\frac{n_t - 1}{n_t + 1}\right)^2$$

The provided equation was used to calculate the metallization criteria factor (M_c), which indicates whether a sample is metallic or insulating.

$$M_c = 1 - \left(\frac{R_m}{V_m}\right)$$

Last but not least, the following formula that describes the bonding nature in the samples was used to calculate the optical electronegativity ($\Delta\chi^*$).

$$\Delta\chi^* = 0.2688\ (E_g)$$

Using the following formulas, the third-order nonlinear optical susceptibility ($\chi^{(3)}$) was also calculated.

$$\chi^{(3)}\ (esu) = \frac{A}{(4\pi)^4}\ (n_t^2 - 1)^4$$

The nonlinear refractive index (n_1) of the glasses was determined using the obtained ($\chi^{(3)}$) value, and the following formula. **Table 5.3** displays the values of $\Delta\chi^*$, $\chi^{(3)}$, and n_1 for each glass sample.

$$n_1(esu) = \frac{12\pi\chi^{(3)}}{n_t}$$

The composition of the glass, the melting temperature, the melting time, the partial pressure of oxygen during melting, the annealing temperature, and the cooling pace are the main elements that affect the absorbance spectra of manufactured glass samples. Base glass exhibits multiple tiny peaks between 231 and 295 nm, a large peak at 310 nm, and smaller peaks at 337 and 371 nm in the UV area (**Fig. 5.7(a)**). It exhibits a peak at around 848 nm in the visible spectrum (**Fig. 5.7(b)**). Strong UV peaks at 318 nm, visible peaks at 415 nm and 950 nm, and near-infrared peaks at 1080 nm, 1240 nm, 1380 nm, 1477 nm, and 1540 nm are all visible in glass doped with 0.5 mol% samarium ions (**Fig. 5.7(c)**). A UV peak at 316 nm, visible peaks at 419 nm and 480 nm, and near-infrared peaks at 1082 nm, 1235 nm, 1378 nm, 1486 nm, and 1740 nm are produced when the samarium content is increased to 1 mol% (**Fig. 5.7(d)**). A single UV peak at 358 nm, visible peaks at 446 nm, 482 nm, and 588 nm, and near-infrared peaks at 1074 nm, 1432 nm, 1525 nm, 1672 nm, 1734 nm, 1888 nm, and 1955 nm are all visible in glass doped with 0.5 mol% praseodymium ions (**Fig. 5.7(e)**). There are visible peaks at 450, 590, and 990 nm, a UV peak at 312 nm, and near-infrared peaks at 1540, 1950, and 2170 nm when 1 mol% praseodymium doping is present (**Fig.**

5.7(f)). These differences in absorption spectra show how various dopant kinds and concentrations affect the glass's optical characteristics at visible, near-infrared, and ultraviolet wavelengths.

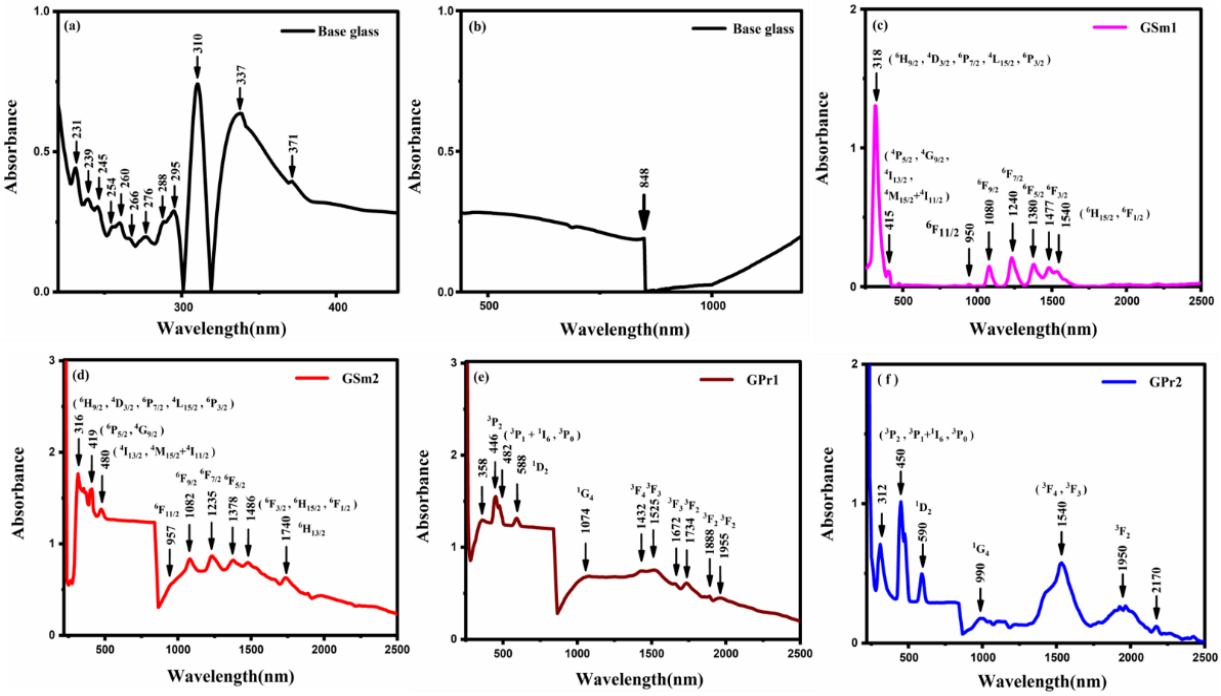

Fig. 5.7. Spectral absorbance of the glass samples: Base glass (a) in the UV and visible range (190–450 nm), Base glass (b) in the visible range, GSm1 (c), GSm2 (d), GPr1 (e), and GPr2 (f) in both the ultraviolet and visible regions.

The glasses doped with samarium and praseodymium ions, the experimental oscillator strengths (f_{exp}) are calculated by integrating the area under their absorption bands using the following formula, where m is the mass of the electron, c is the speed of light, e is the charge of the electron, and $\varepsilon(\nu)$ is the molar absorption coefficient of the band with wave number ν (cm^{-1}).

$$f_{exp} = \frac{2303mc^2}{N_A\pi e^2} \int \varepsilon(\nu)\, d\nu = 4.32 \times 10^{-9} \int \varepsilon(\nu)\, d\nu$$

Additionally, the following formulas, which make use of the Judd-Ofelt theory, are used to derive the calculated oscillator strengths (f_{cal}) for f-f transitions in the absorption bands of these glasses

between the ground state (ΨJ) and the excited state ($\Psi' J'$). Here, J stands for the ground state's total angular momentum (ΨJ), - ν for the transition energy in cm^{-1},

The Judd-Ofelt intensity parameters are - Ω_λ (λ = 2, 4, and 6); the square of the unit tensor's doubly reduced matrix element is denoted as - $\|U^\lambda\|^2$.

$$f_{cal} = \frac{8\pi^2\, mc\nu}{3h(2J+1)} \times \frac{(n_t^2+2)^2}{9n_t} \times \sum_{\lambda=2,4,6} \Omega_\lambda \left(\Psi J \|U^\lambda\| \Psi' J'\right)^2$$

The following formulas are used to determine the Judd-Ofelt parameters Ω_λ (λ = 2, 4, and 6) using a least square fitting approach. This provides a best fit between the experimental oscillator strengths (f_{exp}) and the calculated oscillator strengths (f_{cal}). By utilizing the equation given below to calculate the root-mean-square deviation (σ_{rms}), the correctness of this fitting is evaluated. In this case, σ_{rms} quantifies the accuracy of the computed acquired Ω_λ values; values must normally be less than 1 to have a satisfactory fit quality.

$$\sigma_{rms} = \left[\frac{\sum_{i=1}^{M}\left(f_i^{cal} - f_i^{exp}\right)^2}{M}\right]^{\frac{1}{2}}$$

In conclusion, this approach provides insights into the optical characteristics of the glasses doped with samarium and praseodymium ions by enabling the determination of oscillator strengths by integrating experimental data and theoretical modeling based on Judd-Ofelt theory.

Using an excitation wavelength of 405 nm, the fluorescence spectra of the current Sm^{3+}-doped glass specimen were recorded and are displayed in **Figs. 5.8(a)** and **5.8(b)**. The glass doped with Pr^{3+} exhibits emission spectra in **Figs. 5.8(c)** and **5.8(d)**, respectively.

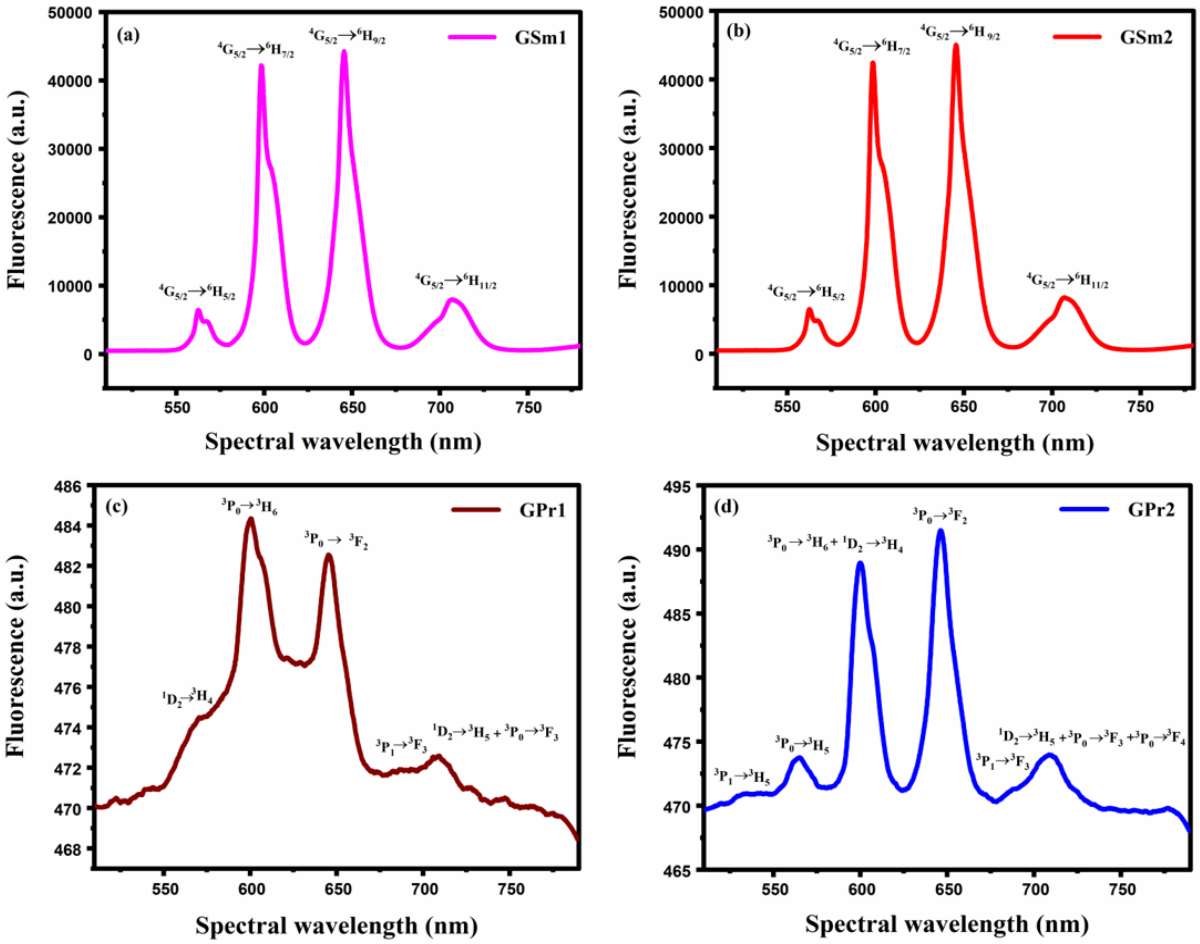

Fig. 5.8. Fluorescence spectra of the glass samples: GSm1 (a), GSm2 (b), GPr1 (c), and GPr2 (d) in the visible region.

The radiative properties of R.E. doped current samples can be calculated using the values of Ω_λ and emission spectrum. Therefore, A_{rad} $(A_{ed} + A_{md})$ is the spontaneous emission probability between the ground state ΨJ and the excited state $\Psi' J'$. The electric and magnetic dipole contributions, represented by $A_{ed}$and A_{md} , respectively, are calculated using the provided formulas.

$$A_{ed} = \frac{64\pi^4 \nu^3 e^2 n_t (n_t{}^2 + 2)^2}{27hc^2\,(2J+1)} \times \sum_{\lambda=2,4,6} \Omega_\lambda \left(\Psi J \left\| U^\lambda \right\| \Psi' J'\right)^2$$

$$A_{md} = \frac{64\pi^4 \nu^3 {n_t}^3}{3h(2J+1)} \times \frac{e^2 h^2}{16\pi^2 m^2 c^2} \times (\Psi J \| L + 2S \| \Psi' J')^2$$

The overall radiative transition probability, or A_T , is calculated as follows totaling all the transitions to the final states:

$$A_T = \sum A_{rad}$$

The values of A_{rad} and A_T can be used to calculate the fluorescence branching ratio or β_r .

$$\beta_r = \frac{A_{rad}}{A_T}$$

The total chance of spontaneous emission for each transition is linked to the radiative lifetime of an emitting state, represented by

$$\tau_{rad} = (A_T)^{-1}$$

The induced emission cross-section σ for each transition is given by

$$\sigma = \frac{\lambda_p^4 A_{rad}}{8\pi c {n_t}^2 \Delta\lambda}$$

Wherein λ_p is the peak wavelength and $\Delta\lambda$ is the peak width at half the maximum of the fluorescence peak for different transitions as determined from the emission spectra.

5.4 Discussions

When rare earth (RE) dopants are added to the glass matrix, the electrical structure of the glass is changed, and this instantly affects the optical properties of the glass, such as spectral substructure and spectrum broadening. The density of the manufactured glass samples ranges from 3.32 to 3.46 $g.cm^{-3}$ and is improved with increasing concentrations of RE spices, indicating a rise in the stiffness of the glasses. Density is a helpful metric for measuring the compactness and concentration of the glass's structure. When samarium and praseodymium ions were added to the glass matrix, the OPD of the current glasses increased from 69.1 to 69.55 ($g.atml^{-1}$). The addition of polar semiconductors and transition metal oxides promoted the formation of a quasiparticle called a polaron, which is the result of interactions between the vibrations of lattice ions and charge

carriers. This affects a variety of processes, including chemical responsiveness, electron transport, and optical absorption [**133**]. When the rare earth ions in the glass matrix increased from 5 to 1 mol%, the prepared samples' polaron radius and interionic distance values decreased from 5.98 to 5.212 $\dot{A}$ and 14.85 to 12.93 $\dot{A}$, respectively, indicating improved tight packing of the obtained glasses. As the glasses become more stiff or compact, their field strength and concentration of rare earth ions increase from 8.307 to 16.81 ($\times 10^{16}$ cm^{-2}) and 3.05 to 4.612 ($\times 10^{20}$ ions cm^{-3}), respectively. The recent investigation also shows the usual inverse pattern of polaron radius and field strength. The amorphous character of the manufactured samples is indicated by the large diffuse hump in the lower region of the X-ray diffraction spectrum of the chosen glass samples in **Fig. 5.3(a)**. An asymmetrical vibration of stretching of the P-O-linkage is the cause of the broad absorption band in the chosen glasses' infrared spectrum, which is situated at about 1100 cm^{-1} [**8**]. The bend vibrates of O-P-O components interspersed with metallic ion oscillations, the distortion mode of P-O-(PO_4^{3-}) groups, the deformation mode of only P-O-(PO_4^{3-}) groups, and the symmetrical and asymmetrical stretching vibrations associated with P-O-P connections are responsible for the medium IR absorption bands located near 474 cm^{-1}, 530 cm^{-1}, and 700 cm^{-1}, respectively [**8**, **134**]. The water, OH, POH, and H_2O molecules are responsible for the absorption bands at 3440 and 1632 cm^{-1}, respectively [**8**]. **Table 5.4** displays the suggested allocation utilized for the analysis of the observed infrared bands. The addition of RE spices, which function as a glass modifier, causes the phonon energy of the glass system to shift to the lower frequency area, occupying the high-frequency band in the base glass's Raman spectra of about 1042 cm^{-1}. The symmetric stretching of non-bridging oxygen on a Q_P^2 tetrahedron, PO_2 symmetric stretching of non-bridging oxygen in Q^2 units, PO_2 symmetric stretching of non-bridging oxygen in Q^1 units, symmetric stretching vibrations of

Table 5.4 FTIR band assignments for all synthesized glass compositions.

Wavenumber(cm^{-1})	Bonding	Sources
474	**The bending vibration of the O-P-O band and (PO_2) modes of $(PO_3)^n$ chain groups overlapped with metal cation vibration, and the deformation mode of P-O-(PO_4^{3-}) groups**	**[8,134]**
530	**the deformation mode of P-O-(PO_4^{3-}) groups**	**[134]**
700	**the ν_s of (P-O-P) groups**	**[134]**
1100	**(ν $(P\text{-}O\text{-}P)_{asym}$) bonding**	**[8]**
1632	**H_2O molecule**	**[8]**
3440	**OH, Water, POH**	**[8]**

PO_3 groups, and $[P_2O_7]^{2-}$ are the reasons behind the bands centering between 858 and 1176 cm^{-1} in the base glass, GSm2, and GPr2 glass system's Raman spectra, respectively.2. Q_P^1 pyrophosphates, terminal $[PO_3]^{2-}$, symmetric stretching of the orthophosphate groups PO_4^{3-}, PO_2- symmetric stretching of the non-bridging oxygen in Q^0 units, asymmetric stretching of P-O-P bridges, and 2-symmetric groups in Q_P^1 pyrophosphates [**135**, **136**]. Furthermore, it was found that the intensities of these bands, which center between 858 and 1176 cm^{-1}, increased in proportion to the amounts of RE-doped ions supplied to the base glass matrix.

When assessing the degree of daylighting in homes, the calculated visible optical characteristics of the glasses under study are essential. Between 42.18 and 47.91%, 43.84 and 57.81%, and.005 and 10.34%, respectively, are these parameters: R_{vis} , T_{vis} , and A_{vis}. When calculating the heat load in homes with different glazing, the computed solar optical properties are important. The respective ranges of the parameters, R_{solar} , T_{solar} , and A_{solar} , are 42.43 to 48.08 percent, 43.76 to 56.28%, and.009 to 10.37 percent. Grid vibrations in the glass network in the infrared region and connecting quasi-anions and cations in the ultraviolet area are the two primary transmission properties that affect the glass system's resulting refractive index [**8**]. As the wavelength and the

concentrations of rare earth ions in the glass matrix increase, it has been observed that the refractive index (n), extinction coefficient (K), real part of the dielectric constant ($\mathcal{E}_R$), and the imaginary part of the dielectric constant ($\mathcal{E}_I$) rise. This has been linked to the formation of non-bridging oxygen. The direct energy gap (E_{gd}) and indirect energy gap (E_{gind}) of the examined samples are determined to be around 2.38 to 3.65 eV and 2.02 to 3.02 eV, respectively. As more RE spices are added to the base glass, the optical energy gap for both the indirect and direct transition of the glasses under research decreases, which also suggests that the glass system is producing more non-bridging oxygen. Depending on the samples' thermal history, the Urbach energy is used to define the degree of disorder in both crystalline and amorphous systems [**65**]. Therefore, the defect concentration might be determined using the Urbach energy value. Urbach energies for the glass samples under study range from .05 to 0.45 eV. The creation of faults in the prepared glasses, which are linked to the creation of localized states in the glasses, causes the Urbach energy values to change. The refractive index of optical glasses is one of its most crucial features. Using the Dimitrov and Sakka relationship, which is additionally impacted by ion polarization, electron density, and molar masses, the mean refractive index (n_t) values of the examined glass samples have been determined [**137**]. All glass samples had n_t values that fall between 2.391 and 2.736. Additionally, it is seen that the addition of RE spices to the glass matrix results in a significant improvement in the n_t values, which suggests the creation of significant polarizable nonbridging oxygen (NBOs) in the glass network. The examined glass samples' molar refraction values, which are proportional to the material's electronic polarizability and directly related to the glass's structure, range from 24.32×10^2 to 26.50×10^2. The electronic polarizability (α_m) of a molecule determines the strength of its electron interactions with an electric field [**104**]. The values of α_m that were obtained range from 9.65×10^2 to 10.51×10^2. The produced glasses' reflection losses

(R_L) and optical transmission (T) vary from.168 to .215 and.64 to .71, respectively. With the addition of RE spices to the glass matrix, the measured values of reflection losses (R_L) and optical transmission (T) rise and fall, respectively, leading one to conclude that these two parameters are inversely related to one another. According to its metallization criterion factor (M_c), a material is either metallic or insulator [**104**]. The condensed matter's Herzfeld metallization hypothesis states that $\frac{R_m}{V_m}$ becomes less than 1 in non-metallic or insulating conditions and more than 1 in metallic conditions [**65**]. Since the obtained values are less than 1, it may be concluded that the synthesized glasses are non-metallic (insulators), as indicated by the existing glasses' M_c values, which vary from 0.31 to 0.38. The obtained values of the optical electronegativity ($\Delta\chi^*$), which range from .53 to .81, give information about the type of bonding present in the samples. The high and low values of $\Delta\chi^*$, respectively, represent the ionic and covalent bonds [**124**]. The values of $\Delta\chi^*$ that we got in this study are shallow, indicating that all the glass samples under evaluation exhibit covalent bonding. The examined glass sample's third-order nonlinear optical susceptibility ($\chi^{(3)}$), measured in esu units, ranges from 3.391× 10^{-12} to 12.095× 10^{-12}. It is seen that the $\chi^{(3)}$ does not exhibit any discernible pattern; rather, the value fluctuates per the concentration of RE ions in the sample. The values of $\chi^{(3)}$show that lone pair electrons increase when RE ions are present. The number of non-bridging oxygen (NBO) in the glass sample affects the obtained values, which range from 5.34× 10^{-11} to 16.65× 10^{-11} for the equivalent nonlinear refractive index (n_1) in the esu unit of manufactured glasses. Significant charge transfer UV absorption bands in the 200–400 nm range are visible in the base glass's UV–visible spectra and these bands are connected to trace Fe^{3+} ions that are present as impurities [**8**]. Peaks in the GSm1 absorption spectra correspond to electronic transitions of Sm^{3+} ions from the ground state, such as $^6H_{5/2}$ to $^6H_{9/2}$ (318 nm), $^4D_{3/2}$ (318 nm), $^6P_{7/2}$ (318 nm), $^4L_{15/2}$ (318 nm), $^6P_{3/2}$ (318 nm), $^4P_{5/2}$ (415

nm), $^4G_{9/2}$ (415 nm), $^4I_{13/2}$ (415 nm), $^4M_{15/2}$+$^4I_{11/2}$ (415 nm), $^6F_{11/2}$ (950 nm), $^6F_{9/2}$(1080 nm), $^6F_{7/2}$(1240 nm), $^6F_{5/2}$(1380 nm), $^6F_{3/2}$(1477 nm), $^6H_{15/2}$(1540 nm), $^6F_{1/2}$(1540 nm). The electronic transitions of Sm^{3+} ions from the ground state are also linked to the peaks found in the GSm2 absorption spectra: $^6H_{5/2}$ to $^6H_{9/2}$(316 nm), $^4D_{3/2}$(316 nm), $^6P_{7/2}$(316 nm), $^4L_{15/2}$(316 nm), $^6P_{3/2}$(316 nm), $^6P_{5/2}$(419 nm), $^4G_{9/2}$(419 nm), $^4I_{13/2}$(480 nm), $^4M_{15/2}$+$^4I_{11/2}$(480 nm), $^6F_{9/2}$(1082 nm), $^6F_{7/2}$(1235 nm), $^6F_{5/2}$(1378 nm), $^6F_{3/2}$(1486 nm), $^6H_{15/2}$(1486 nm), and $^6H_{13/2}$(1740 nm)[**34**,**138**,**139**]. The electronic transitions of Pr^{3+} ions from the ground state, such as $^3H_4$ to $^3P_2$(446 nm), $^3P_1$+$^1I_6$(482 nm), $^3P_0$(482 nm), $^1D_2$(588 nm), $^1G_4$(1074 nm), $^3F_4$(1432 nm), $^3F_3$(1525-1672 nm), and $^3F_2$(1888-1955 nm), are linked to several peaks in the absorption spectra of GPr1 and GPr2 exhibits peaks due to the electronic transitions of Pr^{3+} ions from the ground state, $^3H_4$ to $^3P_2$(450 nm), $^3P_1$+$^1I_6$(450 nm), $^3P_0$(450 nm), $^1D_2$(590 nm), $^1G_4$(990 nm), $^3F_4$(1540 nm), $^3F_3$(1540 nm), and $^3F_2$(1950 nm), as well as one additional peak around 2170 nm [**36**,**140**,**141**]. For analyzing the composition and transition properties of rare-earth ions in the examined glass samples, the Judd-Ofelt intensity parameters Ω_t are essential. Using a least square fitting technique, the electric-dipole contributions of the experimental oscillator strengths were used to determine the parameters Ω_t. The squares of the matrix elements $\left(\|U^\lambda\|^2\right)$ given in Ref. [**142**] were used to do the computation. Tables 5, 6, 7, and 8 display the calculated Ω_2 , Ω_4 , and Ω_6 values of the glasses under study, which are referred to as GSm1, GSm2, GPr1, and GPr2, accordingly. The stiffness of the medium is linked to the Ω_4 and Ω_6 parameters, whereas the glass structure, which depends on R-O covalency around RE^{3+} ions, is linked to the Ω_2 parameter. The GSm1, GSm2, GPr1, and GPr2 samples' parameters show the following pattern: $\Omega_4 > \Omega_2 > \Omega_6$, $\Omega_4 > \Omega_2 > \Omega_6$, $\Omega_6 > \Omega_4 > \Omega_2$, and $\Omega_4 > \Omega_6 > \Omega_2$, respectively. All samples, except sample GPr1, had spectroscopic quality factors $\left(\frac{\Omega_4}{\Omega_6}\right)$ higher than 1, which is a measure of stability. The

glass structure may be used as a candidate for photonics, optoelectronic, and laser modeling applications due to the higher spectroscopic factor values (> 1), which suggest effective stimulated emission in glass materials with excellent stability [**143**, **144**]. The computed spectroscopic value in this case is comparable to those reported for other phosphate glass hosts doped with Pr^{3+} (**Table 5.10**) and Sm^{3+} (**Table 5.9**). The transitions between $^4G_{5/2}$ and $^6H_{5/2}$, $^6H_{7/2}$, $^6H_{9/2}$, and $^6H_{11/2}$, respectively, are responsible for the luminescence peaks of Sm^{3+}-doped glass specimens, which are centered at 562, 600, 646, and 707 nm (**Fig. 5.8(a)** and **5.8(b)**). The allocation of the emission bands was based on earlier reports. The emission that results from doping glass samples that contain borate, phosphate, or fluorophosphate with Sm^{3+} is orange-red [**118**,**152**,**153**]. Similar results were obtained from the manufactured glass samples used in this investigation. The most likely laser transition among these is $^4G_{5/2} \rightarrow {}^6H_{7/2}$, which produces orange emission at 598 nm. Red emission is produced by another strong transition, $^4G_{5/2} \rightarrow {}^6H_{9/2}$, which occurs at 645 nm. Weak emission is produced by $^4G_{5/2} \rightarrow {}^6H_{5/2}$ (565 nm) and $^4G_{5/2} \rightarrow {}^6H_{11/2}$ (711 nm). All the transitions combine to produce an orange-red emission. These emissions are necessary for a wide range of applications, including medical diagnostics, high-density optical storage, underwater communications, and color displays [**118**]. **Fig. 5.9(a)** displays the energy level diagram of Sm^{3+} ions in the current host glass matrix, highlighting the primary emission bands. With an excitation wavelength of 405 nm, the energy levels of Sm^{3+} transition to the beginning states of $^6P_{3/2}$, $^4F_{7/2}$, $^4K_{11/2}$, and $^4L_{13/2}$ after excitation. Subsequently, Sm^{3+}'s energy decreases non-radiatively through phonon vibration energy release, arriving at the lower energy (metastable state) $^4G_{5/2}$. After that, photoemission occurs from the $^4G_{5/2}$ level to other ground levels. The $^4G_{5/2}$ level shows entirely radiative relaxation because it has a sufficiently wide energy gap (more than five phonon energy) in comparison to the next lower level [**139**]. The radiative relaxation of an excited state to all its

lower levels is determined by the values of A_{ed} and A_{md} .While the host-independent matrix elements $\|L+2S\|$ define the values of A_{md} , the energy difference between the beginning and ending levels and the JO parameters determine the values of A_{ed}. Levels with relatively high values of A_{rad} and β_r and energy gaps of more than a few phonons may exhibit laser-made applications. The estimated fluorescence branching ratios and spontaneous-radiative transition rates for the Sm^{3+} transitions $^4G_{5/2} \rightarrow {}^6H_{9/2}$ and $^4G_{5/2} \rightarrow {}^6H_{7/2}$ are substantially higher than those associated with other emission transitions, indicating that these two transitions are like the main Sm^{3+} emission peaks. Sm^{3+} doped glass specimens have the strongest emission band at 645 nm, with a maximum full width at half maximum (FWHM) of 12.38 nm. As the Sm^{3+} concentration increased, it was found that the positions and intensities of the luminescence bands remained constant. Four emission transitions have been observed, as shown in this energy level diagram (**Fig. 5.9(a)**): $^4G_{5/2} \rightarrow {}^6H_{5/2}$, $^4G_{5/2} \rightarrow {}^6H_{7/2}$, $^4G_{5/2} \rightarrow {}^6H_{9/2}$, and $^4G_{5/2} \rightarrow {}^6H_{11/2}$. For every detected emission transition from the $^4G_{5/2}$ level for the Sm^{3+}-doped present phosphate glass matrix, radiative characteristics are measured and listed in Table 11. These include spontaneous emission probabilities (A_{rad}), total radiative transition probability (A_T), luminescence branching ratios (β_r), radiative lifetimes (τ_{rad}), effective emission bandwidths ($\Delta\lambda_{ef}$), and stimulated emission cross-sections (σ). These results indicate that for.5 mol% Sm^{3+} doped glass matrix, the $^4G_{5/2} \rightarrow {}^6H_{7/2}$ emission transition shows the biggest radiative transition among the four, while for 1 mol% Sm^{3+} doped glass matrix, the $^4G_{5/2} \rightarrow {}^6H_{9/2}$ emission transition shows the strongest transitions among the four. The emission transition's lasing potential is described using the branching ratio value. **Table 5.11** shows that among the four transitions, the transition $^4G_{5/2} \rightarrow {}^6H_{7/2}$ for glass specimens doped with .5 mol% Sm^{3+} and the transition $^4G_{5/2} \rightarrow {}^6H_{9/2}$ for glass specimens doped with 1 mol% Sm^{3+} had the biggest branching ratio value. For Sm^{3+}-doped GSm1 and GSm2 glasses with

relatively large values of A_{rad} , the transitions that might exhibit laser activity are $^4G_{5/2} \rightarrow {}^6H_{9/2}$ and $^6H_{7/2}$, respectively. It is discovered that the expected branching ratios are highest for transitions with the largest A_{rad} values. The calculated values of β_r for the GSm1 and GSm2 systems are found to be about $^4G_{5/2} \rightarrow {}^6H_{7/2} > {}^6H_{9/2} > {}^6H_{11/2} > {}^6 H_{5/2}$ and $^4G_{5/2} \rightarrow {}^6H_{9/2} > {}^6H_{7/2} > {}^6H_{5/2} > {}^6 H_{11/2}$, respectively. For both glass systems, the $^4G_{5/2}$ emission transition values of σ fall within the range of 4G5/2 →6H9/2> 6H7/2> 6H11/2 > 6H5/2. The stimulated emission cross-section (σ), which is utilized to identify the potential laser transition in rare-earth-doped glasses, is another important parameter. In both the GSm1 and GSm2 glass systems, the $^4G_{5/2} \rightarrow {}^6H_{9/2}$ transition exhibits the highest σ value, indicating suitability for applications involving reddish-orange laser output. Good laser transitions require a high value of the stimulated emission cross-section. Because they can be used for CW laser operations, materials with a large stimulated emission cross-section (σ) are essential for high gain and low threshold laser applications [**118**]. The GPr1's emission spectra at wavelengths of 570 nm, 600 nm, 645 nm, 686 nm, and 709 nm show five prominent peaks, and these bands correspond to the transitions $^1D_2 \rightarrow {}^3H_4$, $^3P_0 \rightarrow {}^3H_6$, $^3P_0 \rightarrow {}^3F_2$, $^3P_1 \rightarrow {}^3F_3$, and $^1D_2 \rightarrow {}^3H_5 + {}^3P_0 \rightarrow {}^3F_3$ respectively. Six strong peaks at wavelengths of 535 nm, 565 nm, 600 nm, 646 nm, 688 nm, and 708 nm are visible in the GPr2 emission spectra. The transitions $^3P_1 \rightarrow {}^3H_5$, $^3P_0 \rightarrow {}^3H_5$, $^3P_0 \rightarrow {}^3H_6 + {}^1D_2 \rightarrow {}^3H_4$, $^3P_0 \rightarrow {}^3F_2$, $^3P_1 \rightarrow {}^3F_3$, and $^1D_2 \rightarrow {}^3H_5 + {}^3P_0 \rightarrow {}^3F_3 + {}^3P_0 \rightarrow {}^3F_4$ are represented by these bands, respectively [**154-160**]. The energy level diagram of Pr^{3+} ions in the present host glass matrix is shown in **Fig. 5.9(b)**, with the main emission bands highlighted. When stimulated at λ_{ex}= 405 nm , Pr^{3+} ions in the $^3H_4$ ground state are stimulated to the $^3P_2$ state via ground state absorption. After turning off the excitation, these excited ions quickly go through non-radiative relaxation processes to occupy the $^3P_1$, $^3P_0$, and $^1D_2$ metastable states. Following this, photoemission takes place from these metastable levels to other ground states ($^3H_4$, $^3H_5$, $^3H_6$, $^3F_2$, $^3F_3$, $^3F_4$). Because the

energy difference between the $^3P_0$ and the neighboring lower energy ($^3P_1$) states is small, the luminous states thermalize even under ambient conditions. As a result, both excited states begin to produce radiative relaxation ($^3P_0$,1). The energy level diagram (**Fig. 5.9(b)**) shows that the following nine photon emission transitions have been detected in the visible wavelength region: $^3P_1 \rightarrow {}^3H_5$, $^3P_1 \rightarrow {}^3F_3$, $^3P_0 \rightarrow {}^3H_5$, $^3P_0 \rightarrow {}^3H_6$, $^3P_0 \rightarrow {}^3F_2$, $^3P_0 \rightarrow {}^3F_3$, $^3P_0 \rightarrow {}^3F_4$, $^1D_2 \rightarrow {}^3H_4$, and $^1D_2 \rightarrow {}^3H_5$. The Pr^{3+} doped current glass samples exhibit emission transitions of $^1D_2 \rightarrow {}^3H_4$ (orange) and $^3P_0 \rightarrow {}^3H_6$ (red) in the 580–640 nm spectral ranges. The overlap of these two Pr^{3+} ion emission peaks makes it challenging to differentiate and more accurately label the two emission peaks, $^1D_2 \rightarrow {}^3H_4$ (~570-600 nm) and $^3P_0 \rightarrow {}^3H_6$ (~600 nm). Moreover, the relative change in intensities of these two emissions is shown to be dependent on the concentrations of Pr^{3+} ions and the multi-phonon relaxation process at work [**160**]. Additionally, it was observed in the current work from **Figs. 5.8(c)** and **5.8(d)** that for a 0.5 mol% Pr^{3+}-doped glass matrix, the $^1D_2 \rightarrow {}^3H_4$ (orange) transition appeared as a shoulder to the $^3P_0 \rightarrow {}^3H_6$ emission transition, and for a 1 mol% Pr^{3+}-doped glass matrix, it overlapped. Emission intensities were shown to enhance as Pr^{3+} ion concentrations in the present host glass matrix increased by up to 1 mol%. The observed photoluminescence spectra of Pr^{3+}-doped glasses have a complex character due to the overlapping of numerous transitions in a limited region between 510 and 780 nm caused by 4f2→ 4f2 intra-transitions. These emission levels are associated with electronic transitions of the Pr^{3+}ions from the thermally filled $^3P_1$ state and the $^3P_0$ and $^1D_2$ states to lower energy states. As Pr^{3+} concentration increases, the luminescence band positions change and numerous other emission bands are introduced, including $^3P_1 \rightarrow {}^3H_5$, $^3P_0 \rightarrow {}^3H_5$, and $^3P_0 \rightarrow {}^3F_4$. Using three JO parameters, the radiative characteristic parameters required to evaluate the potentiality of the photoluminescence of Pr^{3+} ions in GPr1 and GPr2 glasses are calculated and collected in **Table 5.12**. At a concentration

of 1 mol%, the highest emission intensity was observed at 646 nm ($^3P_0 \rightarrow {}^3F_2$). **Tables 5.9** and **5.10** present a comparison of the estimated radiative lifetimes for samarium and praseodymium ions in the current host glass matrix with those reported in previous studies. **Table 5.10** specifically compares the radiative lifetimes of praseodymium ions originating from the $^3P_0$ energy state.

Table 5.5. Experimental and calculated oscillator strengths for the GSm1 glass samples.

$^6H_{5/2} \rightarrow$	E_{exp} (cm^{-1})	f_{exp}	f_{cal}
$^6F_{1/2}$	6494.55	0.33	0.127
$^6F_{3/2}$	6771.57	0.31	0.582
$^6F_{5/2}$	7247.54	0.32	1.160
$^6F_{7/2}$	8065.81	0.26	0.408
$^6F_{9/2}$	9260.75	0.21	0.095
$^6F_{11/2}$	10528.01	0.03	0.014
$^4I_{13/2}$	24100.27	0.45	0.024
$^4M_{15/2}$	24100.27	0.45	0.007
$^4I_{11/2}$	24100.27	0.45	0.020
$^6H_{9/2}$	31451.61	2.84	0.576
σ_{rms}		$\pm$ 0.8076	
Ω_2 (cm^2)		0.2×10^{-20}	
Ω_4 (cm^2)		1×10^{-20}	
Ω_6 (cm^2)		0.05×10^{-20}	

Table 5.6. Experimental and calculated oscillator strengths for GSm2 glass samples.

$^6H_{5/2} \rightarrow$	E_{exp} (cm^{-1})	f_{exp}	f_{cal}
$^6F_{3/2}$	6731	1.00	1.653

$^6F_{1/2}$	6731	1.00	0.851
$^6F_{5/2}$	7258	1.03	1.620
$^6F_{7/2}$	8098	1.11	1.565
$^6F_{9/2}$	9244	1.05	0.696
$^6F_{11/2}$	10451	0.72	0.108
$^4I_{11/2}$	20837	1.71	0.139
$^6P_{5/2}$	23870	1.80	0.624
$^6P_{7/2}$,$^4P_{3/2}$	31651	2.25	1.193
σ_{rms}		$\pm$ 0.8490	
Ω_2 (cm^2)		1×10^{-20}	
Ω_4 (cm^2)		1.6× 10^{-20}	
Ω_6 (cm^2)		0.3×10^{-20}	

Table 5.7. Experimental and calculated oscillator strengths for GPr1 glass samples.

$^3H_4$ →	E_{exp} (cm^{-1})	f_{exp}	f_{cal}
$^3F_2$	5767.943001	0.26	0.995612
$^3F_3$	6558.434861	0.33	1.811605
$^3F_4$	6984.366734	0.321	1.385737
$^1D_2$	17009.5462	0.576	0.284729
$^3P_1$+$^1I_6$	20750.23478	0.627	1.165871
$^3P_0$	20750.23478	0.627	0.519911
$^3P_2$	22425.14162	0.678	0.91601
σ_{rms}		$\pm$0.784973	
Ω_2(cm^2)		0.2×10^{-20}	
Ω_4 (cm^2)		0.5×10^{-20}	

Ω_6 (cm^2)		1×10^{-20}	

Table 5.8. Experimental and calculated oscillator strengths for GPr2 glass samples.

$^3H_4 \rightarrow$	E_{exp} (cm^{-1})	f_{exp}	f_{cal}
$^3F_2$	5129.032391	0.7875	1.636605
$^3F_4$	6494.554002	1.784	1.321403
$^3F_3$	6494.554002	1.784	2.180989
$^1D_2$	16951.88672	1.74	0.31454
$^3P_1+^1I_6$	22225.80703	3.99	3.513274
σ_{rms}		$\pm$ 0.818752	
Ω_2 (cm^2)		0.1×10^{-20}	
Ω_4 (cm^2)		1.4×10^{-20}	
Ω_6 (cm^2)		1×10^{-20}	

Table 5.9. Judd-Ofelt parameters of Sm^{3+}doped phosphate glasses.

Host glass material	Trend	$\frac{\Omega_4}{\Omega_6}$	τ_{rad} (ms)	Reference
$(ZnO)_{15}(PbO)_{15}(K_2O)_{15}(CaF_2)_9(P_2O_5)_{45.5}$	$\Omega_4 > \Omega_2 > \Omega_6$	20	3.42	Present
$(ZnO)_{15}(PbO)_{15}(K_2O)_{15}(CaF_2)_9(P_2O_5)_{45}$	$\Omega_4 > \Omega_2 > \Omega_6$	5.33	1.03	Present
$(Na_2O)_{45}(Al_2O_3)_2(BaO)_8(P_2O_5)_{45}$	$\Omega_4 > \Omega_6 > \Omega_2$	1.37	2.71	[145]
$(Na_2O)_{42.25}(ZnO)_{15}(P_2O_5)_{42.25}$	$\Omega_6 > \Omega_4 > \Omega_2$	0.62	2.98	[146]
$(Na_2O)_{41.5}(ZnO)_{15}(P_2O_5)_{41.5}$	$\Omega_6 > \Omega_4 > \Omega_2$	0.75	2.51	[147]
$(Li_2O)_{19.5}(CdO)_{20}(P_2O_5)_{60}$	$\Omega_4 > \Omega_2 > \Omega_6$	5.753	1.23	[144]
$(Li_2O)_{19}(CdO)_{20}(P_2O_5)_{60}$	$\Omega_4 > \Omega_2 > \Omega_6$	4.555	1.23	[144]
$(Li_2O)_{17}(Gd_2O_3)_{17}(P_2O_5)_{65}$	$\Omega_2 > \Omega_4 > \Omega_6$	1.70	1.66	[147]
$(ZnO)_{9.46}(PbO)_{24.14}(P_2O_5)_{65.08}$	$\Omega_4 > \Omega_6 > \Omega_2$	2.06	1.29	[143]
$(ZnO)_{20}(PbO)_{20}(P_2O_5)_{59}$	$\Omega_4 > \Omega_6 > \Omega_2$	1.58	9.23	[148]
$(K_2O)_{15}(SrO)_{14.5}(Al_2O_3)_{10}(P_2O_5)_{59.5}$	$\Omega_2 > \Omega_4 > \Omega_6$	1.87	1.67	[149]
$(K_2O)_{17}(Al_2O_3)_9(CaF_2)_{29}(P_2O_5)_{44}$	$\Omega_4 > \Omega_6 > \Omega_2$	1.23	2.93	[150]
$(Na_2O)_{40}(ZnO)_{20}(P_2O_5)_{39}$	$\Omega_4 > \Omega_6 > \Omega_2$	1.31	2.51	[151]
$(K_2O)_{17}(BaO)_{14.5}(Al_2O_3)_9(P_2O_5)_{58.5}$	$\Omega_4 > \Omega_2 > \Omega_6$	1.90	2.09	[139]
$(K_2O)_{17}(BaO)_{11.5}(BaF_2)_6(Al_2O_3)_9(P_2O_5)_{55.5}$	$\Omega_4 > \Omega_2 > \Omega_6$	1.75	2.56	[139]
$(K_2O)_{17}(Al_2O_3)_9(ZnF_2)_{29}(P_2O_5)_{44}$	$\Omega_4 > \Omega_6 > \Omega_2$	1.26	1.61	[152]
$(TeO_2)_{10}(AlF_3)_{20}(LiF)_{19}((NaPO_3)_6)_{50}$	$\Omega_4 > \Omega_6 > \Omega_2$	1.47	2.34	[153]

$(TeO_2)_{10}$ $(AlF_3)_{20}(NaF)_{19}((NaPO_3)_6)_{50}$	$\Omega_4 > \Omega_6 > \Omega_2$	1.32	2.37	[153]
$(TeO_2)_{10}(AlF_3)_{20}(KF)_{19}((NaPO_3)_6)_{50}$	$\Omega_4 > \Omega_6 > \Omega_2$	1.38	2.52	[153]

Table 5.10. Judd-Ofelt parameters of Pr^{3+}doped phosphate glasses.

Host glass material	Trend	$\frac{\Omega_4}{\Omega_6}$	τ_{rad} (μs)	Reference
$(ZnO)_{15}(PbO)_{15}(K_2O)_{15}(CaF_2)_9(P_2O_5)_{45.5}$	$\Omega_6 > \Omega_4 > \Omega_2$	0.5	172.05	Present
$(ZnO)_{15}$ $(PbO)_{15}$ $(K_2O)_{15}(CaF_2)_9(P_2O_5)_{45}$	$\Omega_4 > \Omega_6 > \Omega_2$	1.4	88.38	Present
$(MnCO_3)_5$ $(NaH_2PO_4$, $2H_2O)_{94}$	$\Omega_4 > \Omega_6 > \Omega_2$	1.391	102 ± 9	[154]
$(MnCO_3)_5$ $(NaH_2PO_4$, $2H_2O)_{94.4}$	$\Omega_6 > \Omega_4 > \Omega_2$	0.863	102 ± 9	[154]
$(MnCO_3)_5$ $(NaH_2PO_4$, $2H_2O)_{94.8}$	$\Omega_4 > \Omega_6 > \Omega_2$	1.036	102 ± 9	[154]
$(MnCO_3)_5$ $(NaH_2PO_4$, $2H_2O)_{94.25}$	$\Omega_6 > \Omega_4 > \Omega_2$	0.8066	102 ± 9	[154]
$(Na_2O)_{26}(MgO)_{3.1}$ $(Al_2O_3)_{12.8}(P_2O_5)_{58.1}$	$\Omega_4 > \Omega_2 > \Omega_6$	50.75	185.5	[155]
$(PbO)_{40}(P_2O_5)_{60}$	$\Omega_4 > \Omega_6 > \Omega_2$	1.129	23	[156]
$(MnO_2)_5(P_2O_5)_{94.4}$	$\Omega_6 > \Omega_2 > \Omega_4$	.920	89	[157]
$(MnO_2)_5(P_2O_5)_{94}$	$\Omega_4 > \Omega_2 > \Omega_6$	1.20	86	[157]
$(B_2O_3)_4$ $(Al_2O_3)_7$ $(K_2O)_{10}(BaO)_{17.5}(P_2O_5)_{60}$	$\Omega_4 > \Omega_2 > \Omega_6$	2.415	60	[158]
$(B_2O_3)_4$ $(Al_2O_3)_7$ $(K_2O)_{10}$ $(BaO)_{16.5}(P_2O_5)_{60}$	$\Omega_4 > \Omega_6 > \Omega_2$	1.003	54	[158]
$(CaO)_{25}(BaO)_{15}(SrO)_{15}$ $(P_2O_5)_{44}$	$\Omega_6 > \Omega_4 > \Omega_2$	0.670	25	[159]
$(Na_2O)_6$ $(PbO)_{23.5}$ $(Al_2O_3)_9$ $(K_2O)_{17}$ $(P_2O_5)_{44}$	$\Omega_6 > \Omega_4 > \Omega_2$	.910	7.8	[160]

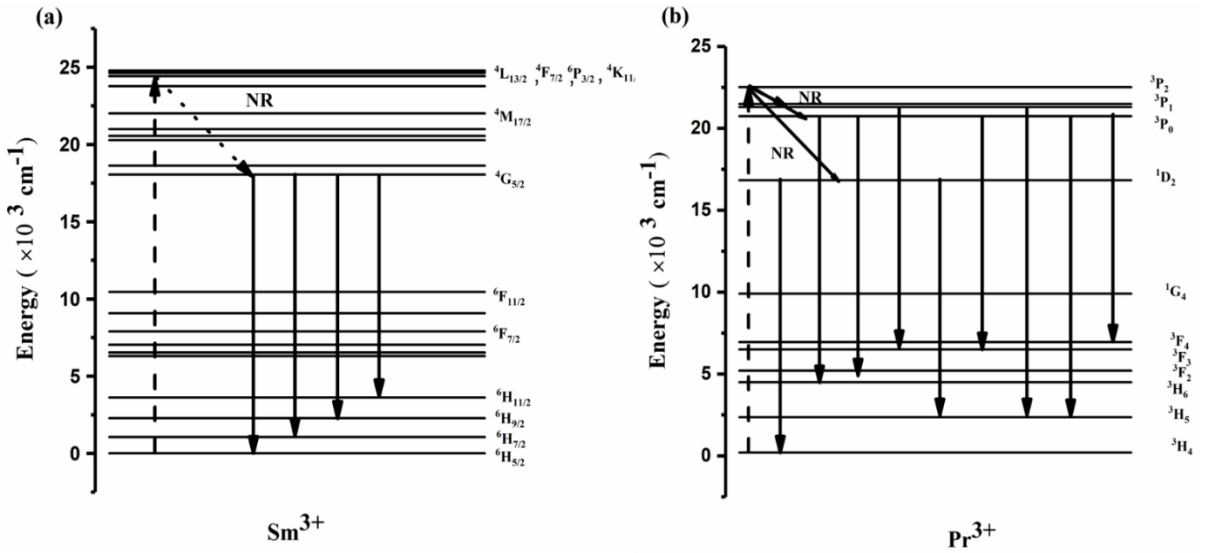

Fig. 5.9. Diagrams illustrating the energy levels and visible emission transitions of Sm^{3+} (a) and Pr^{3+} (b), respectively.

Table 5.11. Laser properties of the glass samples doped with Sm^{3+}.

Glass samples	Transitions	λ_p (nm)	$\Delta\lambda_{ef}$(nm)	A_{rad} (s^{-1})	A_T (s^{-1})	τ_{rad} (ms)	β_r (%)	σ ($\times 10^{-22}$) (cm^2)
GSm1	$^4G_{5/2} \rightarrow {}^6H_{11/2}$	707	23.22	41.39	292.14	3.42	14.16	1.0089
	$^4G_{5/2} \rightarrow {}^6H_{9/2}$	645	12.38	91.88			31.44	2.9137
	$^4G_{5/2} \rightarrow {}^6H_{7/2}$	598	12.00	120.89			41.38	2.9027
	$^4G_{5/2} \rightarrow {}^6H_{5/2}$	562	10.15	37.97			12.99	0.8416
GSm2	$^4G_{5/2} \rightarrow {}^6H_{11/2}$	706	23.02	114.72	969.15	1.03	11.83	2.2014
	$^4G_{5/2} \rightarrow {}^6H_{9/2}$	645	12.33	374.76			38.66	9.3664
	$^4G_{5/2} \rightarrow {}^6H_{7/2}$	598	11.97	360.95			37.24	6.8197
	$^4G_{5/2} \rightarrow {}^6H_{5/2}$	562	10.10	118.70			12.24	2.0752

Table 5.12. Laser properties of the Pr^{3+}-doped examined glass specimens.

Glass samples	Transitions	λ_p (nm)	$\Delta\lambda_{ef}$ (nm)	A_{rad} (s^{-1})	A_T (s^{-1})	τ_{rad} (μs)	β_r (%)	σ ($\times 10^{-20}$) (cm^2)
GPr1	$^3P_1 \rightarrow {}^3F_3$	686.28	14.92	3110.95	3110.952	321.44	100.00	0.9464
	$^3P_0 \rightarrow {}^3H_6$	600.34	31.21	4809.16	5812.036	172.05	82.74	0.4097
	$^3P_0 \rightarrow {}^3F_2$	645.17	14.13	1002.87			17.25	0.2517
	$^3P_0 \rightarrow {}^3F_3$	709.32	41.29	0			0.00	0.0000

	$^1D_2 \rightarrow {}^3H_4$	570.42	7.19	1061.92	1078.929	926.84	98.42	0.3200
	$^1D_2 \rightarrow {}^3H_5$	709.32	41.29	17.00			1.57	0.0021
GPr2	$^3P_1 \rightarrow {}^3H_5$	535.08	27.98	12050.97	15819.730	63.21	76.17	0.7130
	$^3P_1 \rightarrow {}^3F_3$	688.65	10.34	3768.75			23.82	1.6548
	$^3P_0 \rightarrow {}^3H_5$	564.77	31.12	0	11313.700	88.38	0.00	0.0000
	$^3P_0 \rightarrow {}^3H_6$	600.00	16.61	5263.29			46.52	0.8291
	$^3P_0 \rightarrow {}^3F_2$	646.19	16.38	1857.75			16.42	0.3993
	$^3P_0 \rightarrow {}^3F_3$	708.64	36.62	0			0.00	0.0000
	$^3P_0 \rightarrow {}^3F_4$	708.64	36.62	4192.65			37.05	0.5832
	$^1D_2 \rightarrow {}^3H_4$	600.00	16.61	1018.40	1037.412	963.93	98.16	0.1604
	$^1D_2 \rightarrow {}^3H_5$	708.64	36.62	19.00			1.83	0.0026

5.5 Conclusion

The development, characterization, and study of a novel glass matrix containing zinc, lead, potassium, calcium, fluorine, and phosphate modified with various rare earth elements (Pr^{3+}, Sm^{3+}) were successfully proceeded, and all glass samples obtained were found to be homogeneous, transparent, and free of included gases. The glass samples under study have had their physical characteristics identified and explained. The absence of a crystalline peak in the X-ray diffraction measurement clearly shows that the materials under study are amorphous. FTIR and Raman spectroscopy were used to examine the structural features of base glass along with particular glass samples doped with rare earth elements. With the goal of calculating the visible and solar optical characteristics, refractive index, complex dielectric constants, optical band gap energy, and Urbach energy, UV-Visible spectroscopy is utilized in the reflection, transmission, and absorption studies of the related samples. Increasing the quantity of rare earth ions in glasses raises their refractive index, which makes them more optically dispersive. The oxygen packing density, molar refraction, polarizability, reflection loss, optical transmission, metallization criterion, optical electronegativity, and third-order nonlinear optical susceptibility of each of the glass samples under examination have also been determined. All characteristic results demonstrate a strong

relationship between the physical and optical characteristics of every glass under study and the addition of rare earth oxide concentrations. The absorption spectra were used to determine the Judd-Ofelt intensity values Ω_2, Ω_4, and Ω_6 for the base glasses doped with samarium and **praseodymium**, respectively. The laser parameters of the currently studied glasses doped with Sm^{3+} and Pr^{3+}ions were determined using JO parameters and fluorescence data. In general, the findings of this research show that the glasses' high refractive index and good metallization requirements offer a great deal of promise for nonlinear, linear optical switching and optical fiber and photonics and optoelectronics due to their high spectroscopic value. Additionally, these manufactured glasses may be efficiently stimulated by commercial UV and laser diodes, which can subsequently be used to create UV sensors, fluorescent display devices, novel color light sources, and other possible optical and laser technology apparatus.